STABILITY ANALYSIS OF WHIRL FLUTTER IN A ROTOR-NACELLE SYSTEM WITH FREEPLAY NONLINEARITY

Christopher Mair, chris.mair@bristol.ac.uk, PhD Researcher, University of Bristol (UK)

Dr Djamel Rezgui, djamel.rezgui@bristol.ac.uk, Lecturer, University of Bristol (UK)

Dr Branislav Titurus, brano.titurus@bristol.ac.uk, Senior Lecturer, University of Bristol (UK)

Abstract

Tiltrotor aircraft are growing in importance because of their unique flight envelope. However, aeroelastic stability – particularly whirl flutter stability – is a major design influence that requires accurate prediction. Research efforts to make future tiltrotor aircraft larger and faster result in more difficult prediction of whirl flutter onset. Additionally, several nonlinearities that may be present, such as freeplay, are often neglected in analyses for simplicity, or they are investigated using stability analysis methods that do not capture their effects. However these nonlinearities can be significant, sometimes even reversing the stability predictions from linear analysis methods. This paper investigates the effect of a freeplay nonlinearity in the pitch degree of freedom of two rotor-nacelle models of contrasting complexity. The modelling approach and the stability analysis methods employed are explained. Ultimately the freeplay nonlinearity is shown to have a complex effect on the systems' dynamics, including creating the possibility of whirl flutter in parameter ranges that linear analysis methods predict to be stable. This effect is demonstrated via a comparison of stability boundaries for the linear and freeplay versions of the basic model.

1. INTRODUCTION

Tiltrotor aircraft such as the XV-15 shown in Figure 1 aim to combine the speed and range of turboprop aircraft with the VTOL capabilities of helicopters.

Figure 1: XV-15 tiltrotor aircraft [1]

This large and versatile flight envelope makes the tiltrotor configuration highly attractive to both civil and military applications, however a number of

intrinsic engineering challenges are spawned. In addition to the conflicting blade design requirements of hovering efficiency and high forward speed, a powerful design driver is aeroelastic stability. Furthermore, there is a continual push to increase the productivity of available models. Traditionally defined as a function of speed and payload, simultaneous efforts are being made to advance both these aspects. It is however in increasing maximum cruising speed that the aeroelastic instability known as whirl flutter is encountered.

Whirl flutter is an aeroelastic instability that affects propellers or rotors mounted on flexible structures. It is caused by the interaction of elastic wing modes, gyroscopic forces acting on the rotor as a whole and aerodynamic forces and moments acting on the rotor disc. Motion-dependent in-plane forces are the most significant contributor to the instability [2]. The physical origin is coupling between the wing torsional motion and rotor in-plane forces [3]. Additionally, these in-plane forces may destabilise the whole aircraft's short period flight modes [4]. From the designer's perspective, an aircraft's whirl flutter stability is a function of its various physical properties, such as the damping and stiffness of various components or the placement of wing modal frequencies relative to one another. However, from a pilot's perspective, it is encountered at or beyond a certain onset speed.

With slender, highly twisted and flexible blades,

and heavy engine nacelles mounted upon wingtips to provide clearance of the long blades from the fuselage, tiltrotor aircraft are prominently vulnerable to whirl flutter. Whirl flutter limits the performance of tiltrotor aircraft; it either imposes a direct limit on the maximum safe cruise speed, or the increased stiffness (and therefore thickness) of the wings necessary to guarantee aeroelastic stability up to a certain design speed results in reduced aerodynamic efficiency [5]. Accurate prediction of this onset speed is therefore critical: under-prediction causes a waste of potential productivity, while over-prediction places the aircraft at risk of loss.

Several lines of research have been well explored in efforts to attain accurate prediction capabilities of the onset airspeed of whirl flutter in tiltrotors, and also to delay this onset speed and increase stability margins throughout other regions of the flight envelope.

Passive measures constitute making design refinements that act against physical drivers of the whirl flutter instability [8,9]. Active measures on the other hand employ the control of the rotor swashplates or aerodynamic surfaces such as wingtips to delay the whirl flutter onset speed [11,12,13].

While a great deal of work has been devoted to understanding whirl flutter and finding accurate methods of delaying the onset airspeed, the vast majority of the available literature is limited in its treatment of nonlinearities present in real tiltrotor aircraft. In many cases, available studies restricted the modelling of the structural stiffness to linear approximations, which is contingent on the assumption of small deformations. Where nonlinear structural stiffnesses were used, linear stability analysis methods were ultimately employed once linearization about a nonlinear trim point had been obtained. Park et al. investigated whirl flutter with a nonlinear structural model [6], though the focus of the paper was an overall design optimization framework as opposed to any impacts on the whirl flutter predictions made by using nonlinear elements in the model. Additionally, whirl flutter stability analysis in Park's work was conducted using time domain methods. Similarly, investigations by Janetzke et al. [7] used nonlinear aerodynamic models adapted from aerofoil data, though the structural aspects of the model did not appear to have benefitted from the same approach.

However, various kinds of nonlinearity have been shown to have a non-negligible effect on system behaviour. Masarati et al. [8] showed that nonlinear effects at the blade level can have a knock-on effect on overall system stability, and Krueger [9] showed that nonlinearities introduced by the influence of the drivetrain, freeplay and backlash can create a behavioural discrepancy between rotors in windmill and thrust mode. While the main focus of Krueger's paper is to present a multibody modelling approach of an existing ADYN wind tunnel test, the effects of nonlinearity were investigated through the introduction of nonlinear springs in the computational model. Spring stops were also added to provide hard limits on model deflection and a good agreement with the wind tunnel test data was shown. Nonlinear effects are therefore an important modelling consideration, especially in the development of new large tiltrotor aircraft [10,11].

Physical sources of structural nonlinearities in a tiltrotor rotor-nacelle system may be the drivetrain [9], as previously mentioned, though other sources may include the deformability of the rotor blades or joint deadband [8]. The gimbal may itself be a source of structural nonlinearity if elastomeric materials are used therein to provide elastic restraint. Freeplay may exist at hinges and other mechanical interfaces [12], in addition to backlash and saturation nonlinearities. Freeplay is a stiffness nonlinearity where a deadband of highly reduced or zero stiffness exists around the un-deformed equilibrium position. It is only outside of this region that appreciable structural restoring forces act [13], and it is well known to arise in mechanical systems due to ordinary wear. While structural damage may cause a larger freeplay deadband to arise, freeplay oscillations may directly cause the deadband to grow [14]. Lee and Tron [15] demonstrated that the existence of freeplay in a control surface led to a significantly reduced flutter onset speed. In general, the assumption of linear stiffness is only really representative of physical structures when deformations are small – a condition that may well not hold for whirl flutter oscillations – and polynomial softening and/or hardening terms may describe stiffness profiles at larger deflections more realistically [16].

In order to fulfil their flight envelope, tiltrotor aircraft employ nacelle rotation actuators. These actuators are able to rotate each nacelle to any point between horizontal and vertical, and hold the nacelle there. The two-stage telescopic ballscrew design that is typically employed [17] undergoes a range of compressive and tensile loads within one operating cycle. Over time, wear of the lug end that attaches to the nacelle may cause the whole assembly to develop a degree of freeplay. The same effect could also be created through wear or damage of the trunnions that allow the actuator to fit into the wing end via split spindle arms. Freeplay in the nacelle pitch is therefore a plausible eventuality worthy of investigation.

Regardless of what measures have been taken to delay the onset airspeed of whirl flutter, nonlinearities in the system can make linear prediction of this speed inaccurate due to periodic (i.e. whirl flutter) solution branches existing in supposedly stable parameter regions. Compared to the aforementioned linear stability analysis methods, continuation and bifurcation methods are much better suited to the stability analysis of nonlinear systems due to their output of a complete stability "picture" of the system. However, continuation and bifurcation methods are still in the process of proliferation within the field of helicopter dynamics and as a result have so far been limited in their application to a small number of problems [18], such as flight mechanics, ground resonance and rotor vortex ring state. Their inclusion in rotary wing studies is steadily becoming more prevalent as they are powerful when applied to problems such as the identification of instability scenarios of rotor blades [19].

The authors have previously explored the effects of polynomial stiffness nonlinearities on the whirl flutter stability of a basic rotor-nacelle system [20, 21], and a higher fidelity gimballed rotor-wing model [22]. Using continuation methods, it was found that the nonlinearities introduced had a substantial effect on the dynamics of the system as compared to the linear baseline version, sometimes creating the possibility of flutter behaviour when linear analysis predicted stability.

In this paper, two rotor-nacelle models are presented in Section 2. The original formulation as they appear in their respective original literature is given first, followed by details of the freeplay adaptation. Section 3 describes the stability analysis methods used and these are applied to the linear and nonlinear models as appropriate. The analysis was carried out for a number of cases to study the effects of nonlinearity for a set of selected parameters. The stability results and bifurcation diagrams generated are discussed in Section 4.

2. WHIRL FLUTTER MODELS

Two models of contrasting complexity were used for the present research. To illustrate the influence of freeplay on classical whirl flutter, a basic 2-DoF model given by Bielawa [23] and originally formulated by Reed [24] used. For comparison, a more advanced 9-DoF model formulated by Johnson [25] was also used, featuring a gimballed hub, rotor blade dynamics and wing degrees of freedom.

Both models are linear in nature and can therefore be written in the form:

$$\mathbf{M}\ddot{\mathbf{X}} + \mathbf{C}\dot{\mathbf{X}} + \mathbf{K}\mathbf{X} = \mathbf{0} \qquad \{1\}$$

where $\mathbf{M}$ is the mass matrix, $\mathbf{C}$ is the damping matrix and $\mathbf{K}$ is the stiffness matrix. The latter matrices contain both structural and aerodynamic terms.

To facilitate implementation in MATLAB R2015a [26], the models were written in state space-form, shown in Equations {2} and {3}:

$$\dot{\mathbf{Y}} = f(\mathbf{Y}, \mathbf{p}), \quad \mathbf{Y} \in \mathbb{R}^n, \quad \mathbf{p} \in \mathbb{R}^m \qquad \{2\}$$

$$\mathbf{Y} = \begin{bmatrix} \mathbf{X} \\ \dot{\mathbf{X}} \end{bmatrix} \qquad \{3\}$$

where $\mathbf{Y}$ is the state vector, $\mathbf{X}$ is the vector of generalised displacements and $\mathbf{p}$ is the vector of parameters. The generalised displacement vector for each model is provided below in the description of each.

2.1. Basic model

In this model, an N_B-bladed rotor of radius R and moment of inertia about its rotational axis I_x spins with angular velocity Ω about the end of a shaft of length aR rooted at the origin. It is able to oscillate in pitch θ and yaw ψ about the origin with moment of inertia I_n. The dynamical contributions of the wing structure are modelled with lumped stiffness K and damping C properties in the pitching and yawing directions at the effective pivot point. A schematic of this basic system is shown in Figure 2.
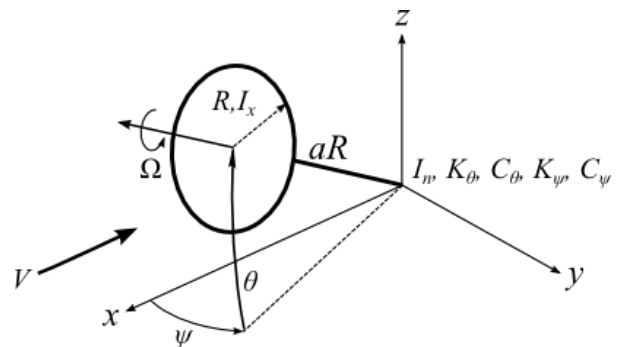

Figure 2: Basic whirl flutter model schematic adopted from [23]

The equations of motion governing the system, as given by Bielawa, are stated in Equation {4}.

$$\begin{bmatrix} I_n & 0 \\ 0 & I_n \end{bmatrix} \begin{bmatrix} \ddot{\theta} \\ \ddot{\psi} \end{bmatrix} + \begin{bmatrix} C_\theta & -I_x\Omega \\ I_x\Omega & C_\psi \end{bmatrix} \begin{bmatrix} \dot{\theta} \\ \dot{\psi} \end{bmatrix}$$
$$+ \begin{bmatrix} K_\theta & 0 \\ 0 & K_\psi \end{bmatrix} \begin{bmatrix} \theta \\ \psi \end{bmatrix} = \begin{bmatrix} M_\theta \\ M_\psi \end{bmatrix} \qquad \{4\}$$

M_θ and M_ψ are aerodynamic moments in pitch and yaw, respectively, and are defined in Equations {5} and {6}. They were derived in the manner employed in Ribner's [27] work on forces and moments generated by propellers experiencing yaw and yawing rates at their hub. Ribner's derivation is founded upon blade element theory and assumes quasi-steady aerodynamics, an aspect that some investigations, such as that by Kim et al [28], have built upon. A key aspect of Ribner's work that separated it from prior art was the inclusion of induction/inflow effects, "analogous to the downwash associated with a finite wing" [27, p. 1]. These equations feature coupling only at the stiffness level, i.e. proportional to angular displacement rather than velocity.

$$M_\theta = \frac{N_B}{2} K_a R \left[-(A_3 + a^2 A_1) \frac{\dot{\theta}}{\Omega} - A_2' \psi + a A_1' \theta \right] \quad \{5\}$$

$$M_\psi = \frac{N_B}{2} K_a R \left[-(A_3 + a^2 A_1) \frac{\dot{\psi}}{\Omega} + A_2' \theta + a A_1' \psi \right] \quad \{6\}$$

Where: $K_a = \frac{1}{2} \rho c_{l_\alpha} R^4 \Omega^2$

K_a is a consolidation of terms for more concise presentation. The A_i terms are aerodynamic integrals that arise from integrating the force expressions along each blade and summing the contributions from each, and can be obtained from [13]. The generalised displacement vector for this basic model is therefore:

$$\mathbf{X} = [\theta \ \psi]^T \quad \{7\}$$

The parameter values used throughout the investigation were retained where possible from Reed [24] and are listed in Table 1. Where ranges of parameters were used, the midpoint value was taken for this parameter set.

Table 1: Datum parameter values used for basic model

Rotor radius	R	0.152 [m]
Rotor angular velocity	Ω	40 [rads^{-1}]
Freestream velocity	V	6.7 [ms^{-1}]
Rotor radius-pivot length ratio	a	0.25 [-]
Number of blades	N_B	4 [-]
Rotor moment of inertia	I_x	0.000103 [kgm^2]
Nacelle moment of inertia	I_n	0.000178 [kgm^2]
Structural pitch damping	C_θ	0.001 [Nmsrad^{-1}]
Structural pitch stiffness	K_θ	0.4 [Nmrad^{-1}]
Structural yaw damping	C_ψ	0.001 [Nmsrad^{-1}]
Structural yaw stiffness	K_ψ	0.4 [Nmrad^{-1}]
Blade chord	c	0.026 [m]

2.2. Gimballed hub model

In this model, an *N*-bladed rotor of radius *R* spins with angular velocity *Ω* at the end of a shaft of length *h*. The shaft is attached to the tip of a single cantilever wing of span *y* that is rigidly supported at its root. The motion of the shaft is expressed in terms of the elastic deformation of the wing and the resulting motion of the wingtip: beamwise/flapwise bending q_1, chordwise bending q_2 and torsion *p*. Modal representations are used for these degrees of freedom. Aggregated damping and stiffness properties are associated with each of these wing degrees of freedom. Additionally, the rotor is attached to the end of the shaft via a gimballed hub, about which the rotor disc may itself pitch and yaw, separately from the motion of the shaft. The flapping and lead-lag motions of the individual blades are summed into multi-blade coordinates using Fourier coefficients to enable transformation from the rotating frame into the non-rotating frame from which the whole system is viewed. The multi-blade flapping of the blades in the non-rotating frame constitutes the aforementioned gimbal pitch and yaw degrees of freedom, β_{1C} and β_{1S} respectively, while the lead-lag is manifested as the rectilinear motion of the rotor's centre of gravity within the hub plane, laterally (ζ_{1C}) and vertically (ζ_{1S}). Collective blade motions are also modelled: as coning β_0 (collective flap) and as rotor speed perturbations ζ_0 (collective lead-lag). The effective stiffnesses of the blade flapping and lead-lag, both cyclic and collective, is modelled implicitly, being specified in terms of the per-rev natural frequency of each motion. The various system components are assigned their own inertial properties. The
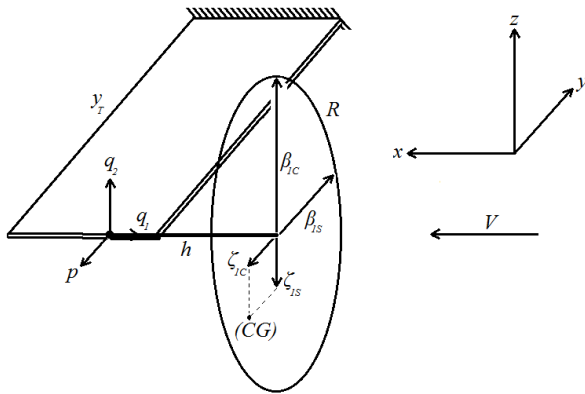
system schematic is shown in Figure 3.

Figure 3: Gimballed hub model schematic adopted from [25].

The aerodynamics of both the blades and the wing are modelled using quasi-steady strip theory [27]. The derivation uses integrals along each blade, summed, and named according to their origin and the direction of their action. The model also allows for the system to perform in both powered and autorotation regimes of operation. Johnson mentions that proprotor dynamics wind tunnel tests at the time of writing frequently operated the rotor in autorotation and uses it as the first point of reference in his results [25]. The present work uses the data pertaining to the powered condition for the purposes of consistency with the basic model and maintaining relevance to real operation of tiltrotor aircraft.

Only the first mode of the blade motions (both flap and lead-lag) and the aforementioned wing motions are considered, due to the assumption that higher modes have negligible participation in the coupled wing-rotor motion. Additionally, the motions are considered to be uncoupled to each other. Also neglected are the aircraft's rigid body motions, since these typically have low frequency and are not strongly coupled with the wing and rotor motions. Modelling the system in this way – as a cantilever wing with a fixed end – is generally representative of the wind tunnel testing configuration of proprotor models at the time the model was developed.

The equations of motion governing the system – obtained by re-deriving the constituent matrices of Equation {198} of [25] with re-inclusion of wing sweep and blade damping terms – are too long to state in the present work. However, adopting their original notation, they can be written in the compact form given in Equation {3}.

The generalised vector for this model is shown in Equation {8}.

$$\mathbf{X} = [\beta_{1C} \quad \beta_{1C} \quad \zeta_{1C} \quad \zeta_{1C} \quad \beta_0 \quad \zeta_0 \quad q_1 \quad q_2 \quad p]^T \quad \{8\}$$

The parameter values used for this model were retained from Johnson [25], and a selection of particularly relevant parameters is listed in Table 2. All dimensionless quantities have been normalised in the same manner as in [25]: rotor quantities with blade inertia I_b and wing quantities with $I_b.N/2$. Johnson gives the parameter values for a wing and two different full-size rotors: a gimballed stiff in-plane rotor and a hingeless soft in-plane rotor. Those describing the former, a 25-ft Bell rotor, have been used here.

Table 2: Datum parameter values used for gimballed hub model

Rotor radius	R	3.82 [m]
Rotor angular velocity	Ω	48.0 [rads^{-1}]
Freestream velocity	V	129 [ms^{-1}]
Rotor shaft length	h	1.31 [m]
Number of blades	N	4 [-]
Wing beam-wise bending stiffness	K_{q1}	18.72 [-]
Wing chord-wise bending stiffness	K_{q2}	50.7 [-]
Wing torsional bending stiffness	K_p	3.595 [-]
Wing beam-wise damping constant	C_{q1}	0.880 [-]
Wing chord-wise damping constant	C_{q2}	2.670 [-]
Wing torsional damping constant	C_p	0.093 [-]
Blade dimensional inertia	I_b	142 [kgm^2]
Blade cyclic flapping inertia	I_β^*	1 [-]
Blade collective flapping inertia	$I_{\beta 0}^*$	0.779 [-]
Blade cyclic lead-lag inertia	I_ζ^*	0.670 [-]
Blade collective lead-lag inertia	$I_{\zeta 0}^*$	1 [-]

2.3. Freeplay adaptation

In their original literature, these models both feature linear structural stiffness. In the nonlinear adaptation of each model, an arctangent expression of the form shown in Equation {9} was implemented [12]. For some deflection quantity α that ordinarily has associated with it some linear restoring force/moment $M=K\alpha$, there exists a deadband with width $2d$ centred about $\alpha=0$. The tuning parameter ε controls the turning radius of the line at the edges of the deadband; the transition

width is approximately 2ε. In addition to controlling the sharpness of the transition, ε also influences the gradient within the deadband, with the gradient approaching zero as ε tends to zero. Outside of this region the stiffness asymptotically approaches the original linear gradient K. As zero ε cannot in practice be used, a non-zero deadband gradient is inevitable. However, using ε=0.00001 results in a deadband gradient of 0.000015 Nmrad^{-1} and 25 Nmrad^{-1} for the gimballed hub model. These values are less than 0.05% of the lowest out-of-deadband gradients considered in both model, and therefore this value was chosen for the present work.

$$M = \frac{K}{\pi}[(\alpha + d)\left(\tan^{-1}\left(-\frac{(\alpha+d)}{\epsilon}\right) + \frac{\pi}{2}\right)$$
$$+ (\alpha - d)\left(\tan^{-1}\left(\frac{(\alpha-d)}{\epsilon}\right) + \frac{\pi}{2}\right)] \qquad \{9\}$$

While some freeplay investigations employ a bilinear stiffness profile, an arctangent profile was chosen here to prevent gradient discontinuities at the deadband limits that may cause difficulties for continuation solvers. Furthermore, deadbands in real freeplay systems are unlikely to be truly non-smooth [12]. Sample profiles are shown in Figure 4, with the original linear stiffness also included for comparison.
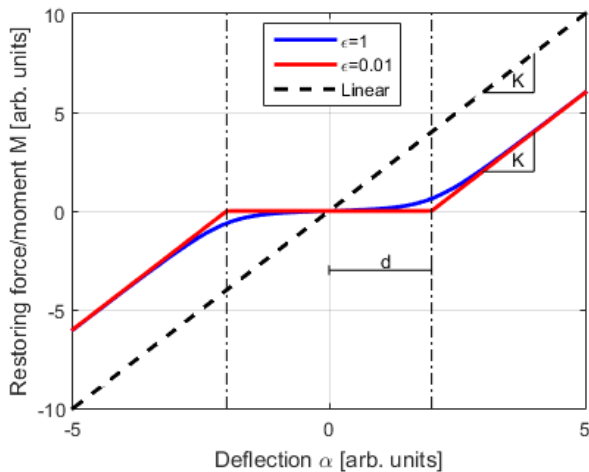

Figure 4: Sample freeplay stiffness profiles as described by Equation {9}, with K=2, ε=[1, 0.01], d=2

The freeplay nonlinearity was implemented in the pitch degree of freedom θ in the basic model, and in the wing torsion degree of freedom p in the gimballed hub model. As the objective of this research is to investigate the impact of freeplay at the rotor tilting mechanism, where it is commonly found, these degrees of freedom were deemed to be the most suitable for model augmentation. The original linear models were used as a baseline for comparison with the nonlinear stiffness adaptations.

3. STABILITY ANALYSIS METHODS

3.1. Linear methods

Initially, eigenvalue analysis was used to assess the stability of the baseline linear version of each model. This standard method places the equations of motion of a system in linear state-space form in order to obtain the Jacobian matrix **J**, defined as:

$$\dot{\mathbf{Y}} = \mathbf{J}\mathbf{Y} \qquad \{10\}$$

where **Y**, the state vector, is defined as in Equation {2}. Given the linear form of the equations of motion of both linear baseline systems, as shown in Equation {3}, the Jacobian matrix for each system is therefore:

$$\mathbf{J} = \begin{bmatrix} \mathbf{0} & \mathbf{I} \\ -\mathbf{M}^{-1}\mathbf{K} & -\mathbf{M}^{-1}\mathbf{C} \end{bmatrix} \qquad \{11\}$$

where **0** and **I** are n x n zero and identity matrices, respectively, where n is the dimension of the vector of generalised displacements of each system. The eigenvalues of the Jacobian matrix contain information about the decay rate (i.e. stability) and frequency of the system's modes, and the corresponding right eigenvectors contain the mode shapes. The undamped natural frequency ω and damping ratio ζ for a given mode are calculated from the real and imaginary parts of its eigenvalue λ using Equations {12} and {13}.

$$\omega = \sqrt{\mathrm{Re}(\lambda)^2 + \mathrm{Im}(\lambda)^2} \qquad \{12\}$$

$$\zeta = \frac{-\mathrm{Re}(\lambda)}{\omega} \qquad \{13\}$$

A negative damping ratio indicates instability of that mode: the growth of oscillation amplitude with time. Only one unstable mode is necessary for overall system instability. Scripts for this eigenvalue analysis were written in MATLAB so that a direct interface with the model was possible.

3.2. Nonlinear methods

For nonlinear systems, numerical continuation and bifurcation theory are used. Continuation is a numerical method that calculates the steady-state solutions of a dynamical system as one of its parameters, called the continuation parameter, is varied [19], constructing solution branches or "continuing" the set of solutions. These solutions can either be fixed points or periodic solutions. Fixed points are considered to be in equilibrium and are analogous to a rigid pendulum standing motionless at either the bottom or top of its arc of motion. Periodic solutions, also known as limit

cycle oscillations (LCOs) are closed trajectories through the state space that return precisely to their starting point and constitute motions that repeat periodically. For each solution point calculated, the stability is then computed. For fixed points, an eigenvalue analysis of the type described in Section 3.1 can be used, requiring local linearization in the case of a nonlinear system. Periodic behaviour on the other hand requires Floquet theory to determine stability [29].

A bifurcation is a qualitative change in the system behaviour due to the variation of a parameter. In other words, when the stability of a system changes, or the type of the solution changes (fixed/periodic), the system bifurcates. The points at which these stability changes happen are called bifurcation points. Another perspective is to consider the phase portraits of the system either side of the bifurcation: they are topologically different and therefore one cannot be mapped to the other through a continuous one-to-one transformation [30]. If the system is nonlinear, new solution branches may emerge from the bifurcation points, leading to the presence of multiple solutions for a given set of system parameters. The identification of these different solution branches helps to uncover the global dynamics of the system. Of particular interest are instances where stability is dependent on the magnitude of a perturbation, a hallmark phenomenon of nonlinear systems.

The results of continuation analysis are displayed on bifurcation diagrams, where the values of solution branches are shown as the continuation parameter value varies. The type (equilibrium/periodic) of each solution branch, along with the location of any bifurcations it encounters, are also indicated. The solutions exist in a space whose number of dimensions is the number of states plus the number of continuation parameters. As this number is almost never less than or equal to the number of spatial dimensions, the convention is to make a 2D graph with the continuation parameter on the x-axis and the chosen state on the y-axis. The plotting of the solutions in terms of the chosen quantity is known as a "projection" or a "plane", e.g. the θ projection, or the K_θ-θ plane. Alternatively, if a 2-parameter continuation is conducted, the results can be plotted on a bifurcation diagram where both axes are parameters.

These analysis methods were employed according to the version of the system (linear/nonlinear) in question. Bifurcation diagrams were produced using the Dynamical Systems Toolbox for MATLAB by Coetzee [31], which uses an implementation of AUTO-07P [32]. Time simulations were also used to corroborate the predictions of both stability

methods. Differing magnitudes of the datum parameter values mean that it is most convenient to deal with normalized quantities. Therefore, for the remainder of the present work all stiffness parameter values discussed refer to their normalised values without a change in notation.

Key bifurcation types that are relevant to understanding the behaviour of a rotor-nacelle system, particularly when the nonlinear stiffness profiles are introduced, are *Hopf bifurcations* and *branch points* [30]. At a Hopf bifurcation, the stability of a fixed point (i.e. an equilibrium) changes, and a periodic solution arises, caused by a pair of complex conjugate eigenvalues crossing the complex plane imaginary axis. At a branch point, the solution changes stability, caused by a single real eigenvalue crossing over the complex plane imaginary axis. Because the branch points observed in the two models presented are of the pitchfork type, two equilibrium branches emanate from the bifurcation point. For more information on the subject, the reader is referred to [30].

4. RESULTS AND DISCUSSION

4.1. Basic model results

At first, the baseline linear version of the basic model is analysed. The un-deformed position of the nacelle (i.e. $\mathbf{X} = \mathbf{0}$) is intuitively an equilibrium that may be used as the initial solution for any continuations. Setting yaw stiffness K_ψ to 0.3 Nmrad^{-1} and performing a continuation in K_θ produces the bifurcation diagram shown in Figure 5.
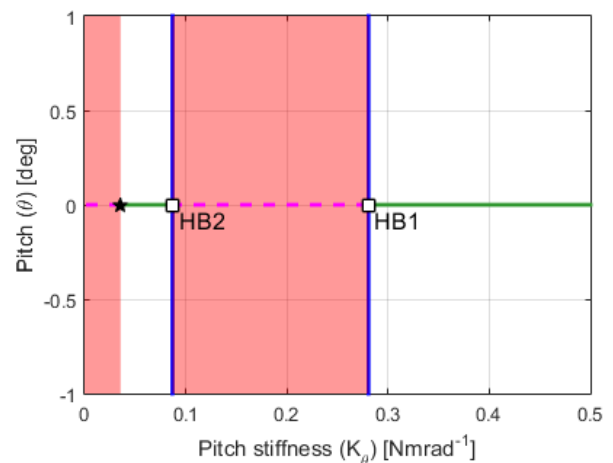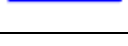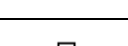

Figure 5: Bifurcation diagram of linear basic model for K_ψ *= 0.3, pitch projection,* K_θ *as the continuation parameter. Regions of instability of the branch shown are shaded red. Hopf bifurcations are labelled "HB"*

Figure 5 shows that the solution remains at 0˚ pitch for the whole continuation, however stability is lost

between the two Hopf bifurcations (square icons) at 0.28 (marked HB1) and 0.09 (HB2), and below ~0.03 following a pitchfork bifurcation. Hopf bifurcations ordinarily indicate the emergence of a periodic solution branch, caused by a complex conjugate eigenvalue pair crossing the imaginary axis. However, as the system is linear, no uniquely defined LCOs exist. Instead, an infinitely large family of flutter-like oscillations emanates from each of the Hopf bifurcations. Their amplitudes are defined by the initial conditions used to simulate them in numerical integration, and they exist entirely at the K_θ value at which their originating Hopf bifurcation is located. This is indicated by the vertical blue lines connected to each Hopf bifurcation. At all values in between 0.09 and 0.28, the whirl flutter motion is of unbounded amplitude. The pitchfork bifurcation at K_θ=0.03 indicates the emergence of further fixed point solution branches. In practice, this means static divergence of the nacelle as it is pushed to the side by aerodynamic moments. The entire un-deformed equilibrium branch shown in Figure 5 will be termed the "main branch" in the present work. A key to the symbols and line colours used in the bifurcation diagrams shown in this paper is given in Table 3.

Table 3: Key to symbols and line colours used in bifurcation diagrams in this paper

———	Solid green line	Stable equilibrium branch
– – –	Dashed magenta line	Unstable equilibrium branch
———	Solid blue line	Stable periodic solution branch
··············	Dotted red line	Unstable periodic solution branch
□	Hollow square	Hopf bifurcation
★	Black star	Branch point bifurcation
●	Black circle	Limit point (fold) bifurcation
▲	Black triangle	Homoclinic bifurcation

A stability boundary between K_θ and K_ψ, shown in Figure 6, can be constructed by performing two-parameter continuations to trace the loci of the aforementioned bifurcations within the K_θ-K_ψ plane. This boundary could be generated by applying the linear methods discussed in Section 3.1 to each point in the K_θ-K_ψ plane and joining all points found to have neutral stability. However, using

continuation methods affords the insight of mapping out the parameter value regions of specific types of instability.
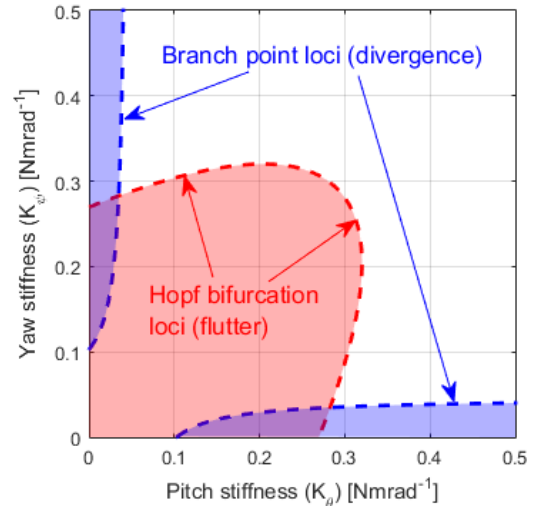

Figure 6: Stability boundary between pitch stiffness K_θ and yaw stiffness K_ψ, generated by two-parameter continuation. All shaded areas are unstable

All the shaded areas in Figure 6 are subject to an instability; all points within the red region will experience flutter, while all points within the blue lobes will experience static divergence. Having established this stability boundary as a baseline, the freeplay nonlinearity discussed in Section 2.3 may be introduced.

In the freeplay model, the un-deformed position $\mathbf{X} = \mathbf{0}$ is uniformly unstable for all values of K_θ due to the effectively zero pitch stiffness there. For non-trivial continuation results a new equilibrium must be found for the initial solution. The nacelle must lie at some pitch angle outside of the deadband, where the structural restoring moment is non-zero and able to oppose the aerodynamic moments that act to push the nacelle further away from the undeflected position. Being deflected in pitch, the nacelle in turn experiences an aerodynamic yaw moment pushing it away from $\mathbf{X} = \mathbf{0}$ that must be countered by yaw structural stiffness. This new non-zero branch of equilibrium solutions can be found by solving the equations of motion with all time derivatives set to zero. Two exist, mirrored in θ and ψ due to the structural symmetry of the system, and will be referred to as the non-zero main branches for the remainder of the present work.

Using a deadband half-width d of 0.1˚, a continuation in K_θ identical to that shown for the linear system in Figure 5 is now performed and

shown in Figure 7. The periodic solution branches emanating from the Hopf bifurcations are also shown. It is common in bifurcation analyses to indicate periodic solution branches by the maximum (i.e. most positive) state value in the LCO at each parameter value. For clarity in the present work, the minimum value of each LCO branch is also indicated. A thick line is used for the maximum values, and a thinner line for the minimum values.
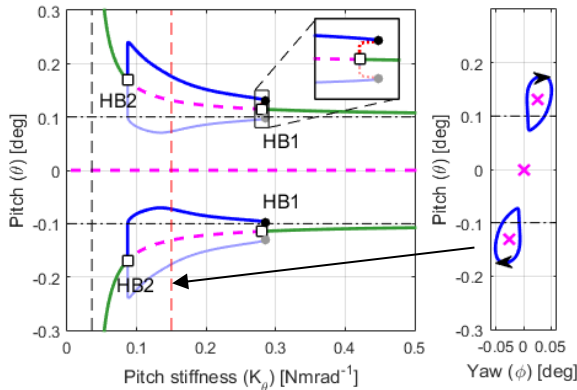

Figure 7: (left) Bifurcation diagram of freeplay basic model for K_Ψ = 0.3, d=0.1˚, pitch projection, K_θ as the continuation parameter. The K_Ψ value of the linear system's pitchfork bifurcation is indicated with a vertical dashed black line. (right) phase plane at K_θ=0.15 (dashed red line). The freeplay deadband is indicated with a dash-dot black line in both plots

The first notable feature of Figure 7 is that for most of the range of the continuation parameter, three main solution branches exist instead of one as in the linear model. On the left side of the figure, the two new non-zero main branches reach infinitely large solution values with decreasing K_θ. Interestingly, this runaway to infinity is asymptotic to the K_θ value of the pitchfork bifurcation in the linear system (~0.03). The Hopf bifurcations on these two new branches are the same as those observed in Figure 5 and are unchanged in their K_θ location. A small stable (i.e. attracting) flutter branch is attached to each non-zero main branch at the Hopf bifurcations. A phase plane of the two flutter branches at K_θ=0.15 is shown in the right plot. Their maximum and minimum values can be cross-referenced with the left plot, along with the positions of the zero and non-zero main branches. Where each flutter branch joins the right-most Hopf at ~0.28, it first overhangs the stable non-zero main branch by a small amount, shown in the zoomed inset box in the left plot. In plain terms, this means that flutter is possible for a slightly larger range of parameter values than the linear analysis predicts.

As is evident here, bifurcation analysis is powerful in its ability to uncover the full structure of steady state solutions of a dynamical system. While the

eigenvalues and Floquet multipliers do give an quantitative indication of stability close to the solution branches, continuation results alone are not sufficient to predict transient behaviour reliably. Therefore, it is common to complement bifurcation analysis with time domain simulations (i.e. numerical integrations of the equations of motion) at selected system configurations. Figure 8 shows the same bifurcation diagram as that in upper half-plane of Figure 7, however time simulations in the pitch state θ for two selected points are also shown.

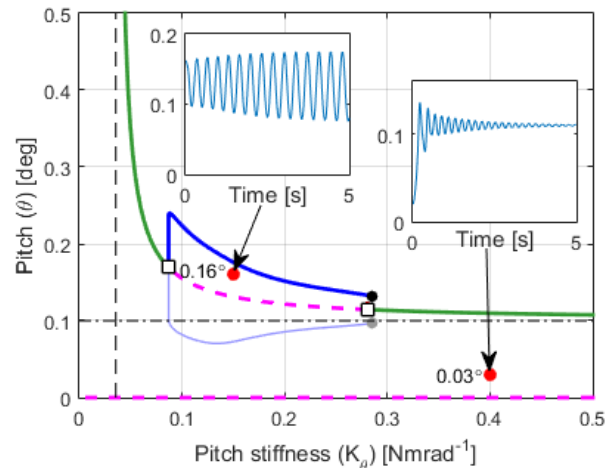*Figure 8: Bifurcation diagram of freeplay basic model for K_Ψ = 0.3, d=0.1˚, pitch projection. Time simulations are shown in inset windows, with initial conditions indicated by red dots.*

As the non-zero main branches (and their attached flutter branches) are completely symmetrical, only the positive pitch branch is shown for the remaining figures, for simplicity. Convergence on the stable flutter branch attached to the positive non-zero main branch is shown on the left of the figure. Divergence away from the unstable zero (equilibrium) main branch and convergence on the stable non-zero main branch is shown on the right.

As K_Ψ is lowered (moving downward on Figure 6), HB2 moves leftward in K_θ and HB1 moves rightward. Furthermore, the flutter branches grow in amplitude, reaching toward the unstable zero-branch. Their eventual collision with the zero-branch happens simultaneously due to the symmetry of the system. At this collision point, the two flutter LCOs make contact with each other at the unstable zero branch. The resulting orbit of infinite period that is created links the central fixed point to itself, and is known as a homoclinic trajectory. The fusing of orbits to form such a trajectory is known as a homoclinic bifurcation. It occurs below K_Ψ=0.28, when HB2 is no longer present to re-attach the flutter branches to the non-zero main branches. A continuation in K_θ with K_Ψ

set to 0.2 is shown in Figure 9, to demonstrate the presence of the homoclinic collision.
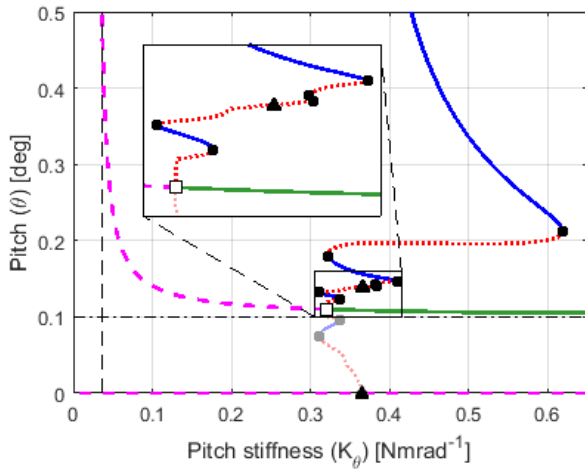

Figure 9: Bifurcation diagram of freeplay basic model for $K_\Psi = 0.2$, d=0.1˚, pitch projection, K_θ as the continuation parameter. Magnification of the region surrounding the homoclinic collision (black triangle) is shown in inset.

At K_θ values above the homoclinic collision point (~0.366), a single new LCO exists which, near the collision, resembles a bowtie. It is a product of the fusing of the two flutter branches, and is of comparatively large amplitude. A phase portrait of the trajectories before, during and after fusing is shown in Figure 10.
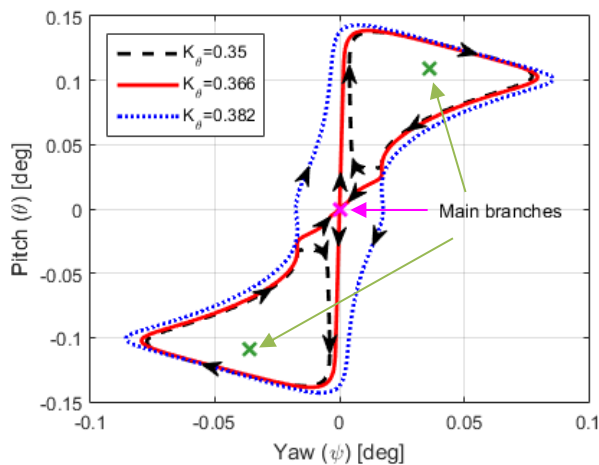

Figure 10: Phase portraits of the two flutter branches before (dashed black), during (solid red) and after (dotted blue) fusing into a single LCO at the homoclinic collision point. Main branch fixed point equilibria at the homoclinic point K_θ=0.366 are indicated with 'X' icons.

As Figure 9 shows, the "bowtie" LCO branch folds back and forth between $K_\theta = 0.32$ and 0.62 as it increases in amplitude. However, it can also be seen that throughout this parameter range, the non-zero main branches are stable, and ordinarily

it is only these branches that constitute stability analysis. That is, linear stability analysis would declare this parameter range to be stable, despite the presence of the "bowtie" LCO there. The hazard posed by this branch is therefore threefold: it has a comparatively large amplitude, is largely stable (and therefore attracts), and overhangs the non-zero main branches at K_θ values as high as 0.62 – well into the supposedly stable region of the stability boundary. The two parts of this LCO branch that are present at $K_\theta = 0.55$ are shown in a phase plane, in the lower part of Figure 11. A smaller unstable LCO with an amplitude of ~0.25˚ is surrounded by a larger, stable LCO with an amplitude of ~0.3˚.

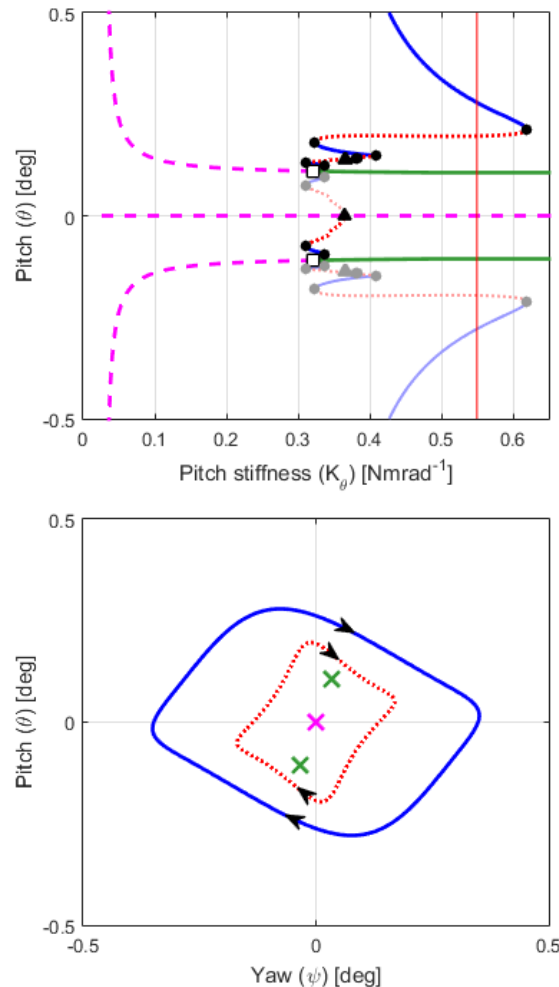

Figure 11: (lower) phase plane of bowtie LCO at K_θ =0.55. (upper) the location of the phase plane in the pitch projection is shown with a solid red line

The fact that the overhanging branch is stable means that the system is able to be attracted to it following a sufficient perturbation. In practical terms, such a perturbation might be provided by a gust, or by manoeuvring. Figure 12 shows two time simulations with K_ψ=0.2, K_θ=0.55 (the same

parameter values of the "slice" taken in Figure 11), showing one insufficient perturbation causing the system to join the upper non-zero main branch (red line), and a similar but sufficient perturbation causing the system being attracted to the bowtie LCO (blue line).
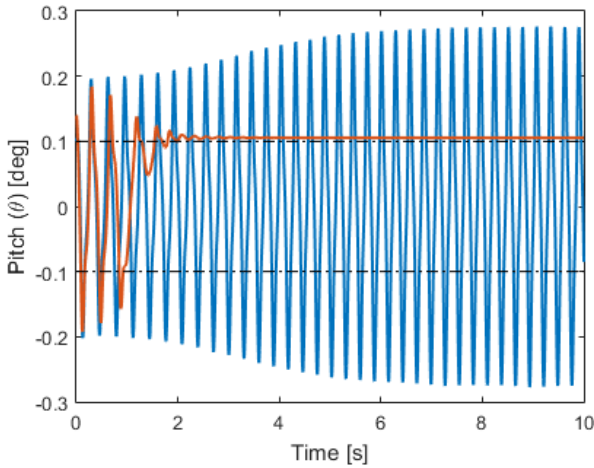

Figure 12: Time simulations with K_ψ=0.2, K_θ=0.55. Depending on the perturbation supplied as the initial conditions, the system can join one of the non-zero main branches (red line) or join the bowtie LCO (blue).

The existence of the bowtie LCO – specifically created by the presence of the freeplay nonlinearity – is the significant problem. In practical terms, a significant whirl flutter oscillation is possible in parameter ranges declared safe by linear stability analysis. The extent of the overhang in K_θ of this LCO over the non-zero main branches – and therefore its intrusion into the stable region of the stability boundary – can be tracked in the K_θ-K_ψ plane. This redrawn stability boundary is shown in Figure 13.
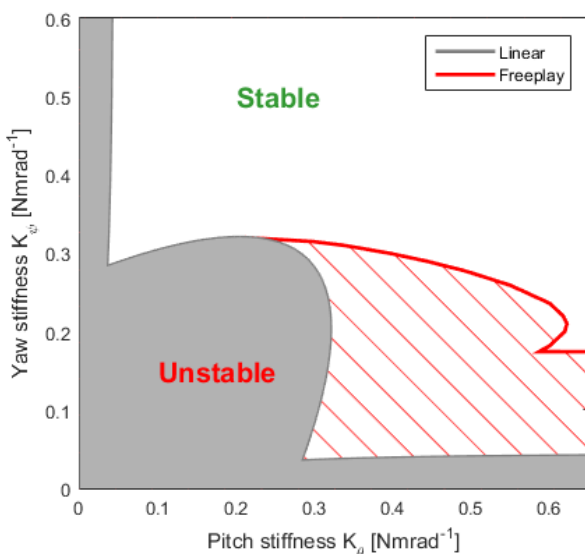

Figure 13: Redrawn stability boundary for basic freeplay system, based on overhang of bowtie LCO.

4.2. Gimballed hub model results

Though much more complex, the gimballed hub model reacts to the freeplay nonlinearity in much the same way as the basic model. The deadband causes the un-deformed zero branch to become uniformly unstable, and creates two non-zero equilibrium branches. While a multi-case dynamical analysis of the gimballed hub model is not shown here, attention is instead drawn to the existence of the same phenomenon detailed in Section 4.1. Specifically, a stable bowtie LCO branch is shown to also exist in the gimballed hub model. Figure 14 shows the stability boundary between wing torsional stiffness K_p and wing chordwise bending K_{q2}. Overlaid is a selection of time histories in wing torsion angle p, pertaining to supposedly stable points in the parameter space. The blue lines shows the response of the freeplay model with d=0.1˚, and for comparison the red lines show the response of the linear model with the same configuration. In both cases, the linear model quickly settles on the zero main branch, which at these parameter values is stable. However, the freeplay model is attracted to the bowtie LCO in both cases. The linear model is not capable of such behaviour, and as such it is directly attributable to the presence of the freeplay nonlinearity applied to the wing torsion degree of freedom p.
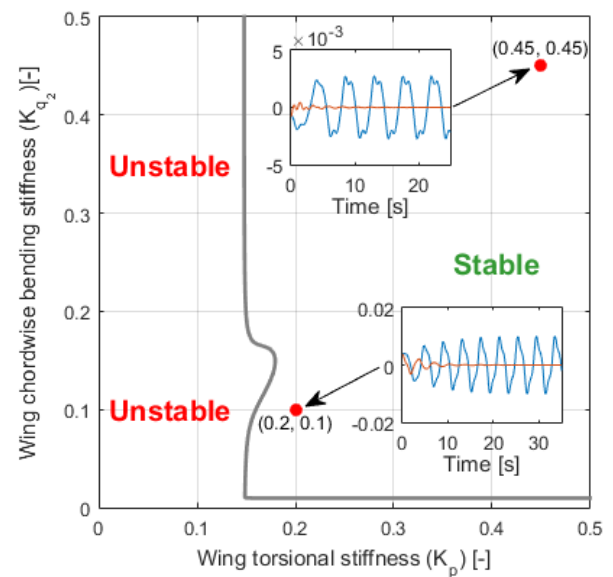

Figure 14: Stability boundary of gimballed hub model between wing torsional stiffness and wing chordwise bending stiffness, with insets showing time histories of wing torsion angle p for the freeplay model (blue) and linear model (red). Initial conditions shown with red dots.

5. CONCLUSIONS

This article has demonstrated the use of continuation and bifurcation methods to provide nonlinear dynamic analysis of whirl flutter. Freeplay

is inevitable in mechanical systems due to wear and therefore may arise in tiltrotor nacelle tilting mechanisms. To investigate the impacts of such freeplay on whirl flutter predictions, two rotor-nacelle system models of contrasting complexity were implemented, using both linear and freeplay stiffness profiles for the pitch degree of freedom in in each model. The freeplay expression used arctangent terms to create a smooth-edged deadband in an otherwise quasi-linear profile. Appropriate stability analysis methods were described and employed for both the linear and nonlinear models. Bifurcation diagrams were generated for a number of pitch stiffness cases for the basic model.

While the introduction of the freeplay deadband significantly altered the topology of the bifurcation diagrams relative to the linear cases, the most crucial effect was the creation of a large, attracting whirl flutter branch termed the "bowtie" LCO on account of its appearance. This large LCO was shown to exist for an expansive range of parameter values in the basic model that linear analysis claims to be stable. A revised stability boundary based on this phenomenon was generated for the basic model and the size of the unstable region was shown to grow considerably as a result. The gimballed hub model was also shown to develop stable bowtie LCO branches as a result of freeplay being present.

The findings also show that the presence of freeplay in a system can invalidate previous guidance regarding structural stiffness. Reed notes in some of his literature [24] that the elongation of the Hopf-bulge (as seen in Figure 6) along its axis of symmetry means that having particularly dissimilar values of pitch and yaw stiffness can give a greater stability margin. However, in the case of low yaw stiffness, very much the opposite was found in the present work.

Important of note is that the prediction of the large LCO to be stable is not an indication that encountering it is safe, but rather that the LCO is able to attract the system to it. Upon entering the LCO, the large oscillation amplitudes would likely cause a rapid degradation in the structural properties of the aircraft, most likely leading to structural failure. Even if this degradation were not to occur immediately, the oscillations would present a fatigue hazard to aircraft nacelle mounts.

In further work, it is anticipated that a revised stability boundary will be generated for the gimballed hub model. Refinements to the aerodynamic modelling employed in both models would also be a sensible development.

6. ACKNOWLEDGMENTS

REFERENCES

[1] NASA, Photo ID EC80-75, public domain.

[2] Nixon M. W., *Parametric Studies for Tiltrotor Aeroelastic Stability in Highspeed Flight*, J. Am. Helicopter Soc. 38(4) pp. 71-79, 1993

[3] Popelka D., Sheffler M., Bilger J., *Correlation of Test and Analysis for the 1/5-Scale V-22 Aeroelastic Model*, J. Am. Helicopter Soc. 32(2) pp. 21-33, 1987

[4] Quigley H. C., Koenig D. G., *A Flight Study of the Dynamic Stability of a Tilting-Rotor Convertiplane*, NASA TN D-778, 1961

[5] Peyran, R. J., Rand O., *Effect of design requirements on conceptual tiltrotor wing weight*, American Helicopter Society 55th Annual Forum, Montréal, Canada, 1999

[6] Park J. S., Sung N. J., Myeong-Kyu L., Kim J. M., *Design Optimization Framework for Tiltrotor Composite Wings Considering Whirl Flutter Stability*, Composites Part B: Engineering 41(4) pp. 257-267, 2010

[7] Janetzke D. C., and Kaza K. R. V., *Whirl Flutter Analysis of a Horizontal-axis Wind Turbine with a Two-bladed Teetering Rotor*, Solar Energy 31(2) pp. 173-182, 1983

[8] Masarati P., Piatak D. J., and Quaranta G., *Soft-inplane Tiltrotor Aeromechanics Investigation Using Two Comprehensive Multibody Solvers*, J. Am. Helicopter Soc. 53(2) pp. 179-192, 2008

[9] Krueger W. R., *Multibody Analysis of Whirl Flutter Stability on a Tiltrotor Wind Tunnel Model*, Proc. of the Institution of Mechanical Engineers, Part K: Journal of Multi-body Dynamics 230(2) pp. 121-133, 2014

[10] Acree C. W., Johnson W., *Performance, Loads and Stability of Heavy Lift Tiltrotors*, AHS Vertical Lift Aircraft Design Conference, San Francisco, CA, USA, 2006

[11] Acree C. W., Johnson W., *Aeroelastic Stability of the LCTR2 Civil Tiltrotor*, AHS Technical Specialists' Meeting, Dallas, TX, USA, 2008

[12] Howcroft, C., et al., *Shimmy of an Aircraft Main Landing Gear with Geometric Coupling and Mechanical Freeplay*, J. Comput. Nonl. Dyn. 10.5 p. 051011, 2015

[13] Garrick I., Reed W. H. III, *Historical Development of Aircraft Flutter*, J. Aircraft 18(11) pp. 897-912, 1981

[14] Padmanabhan M. A., *Sliding Wear and Freeplay Growth due to Control Surface Limit Cycle Oscillations*, J. Aircraft (Article in Advance) pp. 1-7, 2019

[15] Lee B.H.K., Tron A., *Effects of Structural Nonlinearities on Flutter Characteristics of the CF-18 Aircraft*, J. Aircraft 26(8) pp. 781-786, 1989

[16] Jutte C.V., Kota S., *Design of Nonlinear Springs For Prescribed Load-Displacement Functions*, J. Mech. Des. 130(8) 081403, 2008

[17] White G., *A Tilt-rotor Actuator*, Proc. IMechE 224 G: Aero. Eng., 2009

[18] Rezgui D., Lowenberg M. H., *On the Nonlinear Dynamics of a Rotor in Autorotation: a Combined Experimental and Numerical Approach*, Phil. Trans. R. Soc. A, 373.2051 20140411, 2015

[19] Rezgui D., Lowenberg M. H., Jones M., Monteggia C., *Continuation and Bifurcation Analysis in Helicopter Aeroelastic Stability Problems*, J. Guid. Control Dyn. 37 pp. 889–897, 2014

[20] Mair C., Rezgui D., Titurus B., *Nonlinear Stability Analysis of Whirl Flutter in a Tiltrotor Rotor-Nacelle System*, Proc. 43rd European Rotorcraft Forum, Milan, Italy, 2017

[21] Mair C., Rezgui D., Titurus B., *Nonlinear Stability Analysis of Whirl Flutter in a Rotor-Nacelle System*, J. Nonl. Dyn. 94(3) pp. 2013-2032, 2018

[22] Mair C., Rezgui D., Titurus B., *Stability Analysis of Whirl Flutter in a Nonlinear Gimballed Rotor-Nacelle System*, Vertical Flight Society 75th Annual Forum, Philadelphia, PA, USA, 2019

[23] Bielawa R. L., *Rotary Wing Structural Dynamics and Aeroelasticity*, Second Edition, Washington, DC: American Institute of Aeronautics and Astronautics, p389, 2005

[24] Reed W. H. III, Bland S. R., *An Analytical Treatment of Aircraft Propeller Precession Instability*, NASA TN D-659, 1961

[25] Johnson W., *Dynamics of a tilting proprotor aircraft in cruise flight*, NASA Technical Note D-7677, 1974

[26] MATLAB 2015a: The MathWorks Inc., Natick, Massachusetts, USA

[27] Ribner H. S., *Propellers in Yaw*, NACA Report 820, 1945

[28] Kim T., Shin S. J., Taehyoun K., *Analysis of tiltrotor whirl flutter in time and frequency domain*, J. Mech. Sci. Tech. 23(12), pp. 3281-3291, 2009

[29] Kuchment P. A., *Floquet Theory for Partial Differential Equations*, Vol. 60. Birkhäuser, Basel, 2012

[30] Kuznetsov Y. A., *Elements of Applied Bifurcation Theory*, Third Edition, Vol. 112. Springer Science & Business Media, 2004

[31] Coetzee, E., Krauskopf, B., Lowenberg, M., *The dynamical systems toolbox: Integrating AUTO into MATLAB*, Proc. 16th US National Congress of Theoretical and Applied Mechanics USNCTAM2010-827, 2010

[32] Doedel E. J., Fairgrieve T. F., Sandstede B., *AUTO-07P: Continuation and bifurcation software for ordinary differential equations*, 2007